

Coherent inverse Compton scattering by bunches in fast radio bursts

BING ZHANG¹

¹*Department of Physics and Astronomy, University of Nevada, Las Vegas, Las Vegas, NV 89154, bing.zhang@unlv.edu*

ABSTRACT

The extremely high brightness temperature of fast radio bursts (FRBs) requires that their emission mechanism must be “coherent”, either through concerted particle emission by bunches or through an exponential growth of a plasma wave mode or radiation amplitude via certain maser mechanisms. The bunching mechanism has been mostly discussed within the context of curvature radiation or cyclotron/synchrotron radiation. Here we propose a family of model invoking coherent inverse Compton scattering (ICS) of bunched particles that may operate within or just outside of the magnetosphere of a flaring magnetar. Crustal oscillations during the flaring event may excite low-frequency electromagnetic waves near the magnetar surface. The X-mode of these waves could penetrate through the magnetosphere. Bunched relativistic particles in the charge starved region inside the magnetosphere or in the current sheet outside of the magnetosphere would upscatter these low-frequency waves to produce GHz emission to power FRBs. The ICS mechanism has a much larger emission power for individual electrons than curvature radiation. This greatly reduces the required degree of coherence in bunches, alleviating several criticisms to the bunching mechanism raised in the context of curvature radiation. The emission is $\sim 100\%$ linearly polarized (with the possibility of developing circular polarization) with a constant or varying polarization angle across each burst. The mechanism can account for a narrow-band spectrum and a frequency downdrifting pattern, as commonly observed in repeating FRBs.

Keywords: fast radio bursts – radio transient sources – magnetars

1. INTRODUCTION

Fast radio bursts (FRBs) (Lorimer et al. 2007; Petroff et al. 2019; Cordes & Chatterjee 2019; Zhang 2020) have a brightness temperature

$$T_b \simeq \frac{S_{\nu,p} D_A^2}{2\pi k_B (\nu \Delta t)^2} = (1.2 \times 10^{36} \text{ K}) \times D_{A,28}^2 (S_{\nu,p}/\text{Jy}) \nu_9^{-2} \Delta t_{-3}^{-2}, \quad (1)$$

where k_B is Boltzmann constant, $S_{\nu,p}$ is specific flux at the peak time, ν is observing frequency, Δt is variability timescale, D_A is angular distance of the source, and the convention $Q_n = Q/10^n$ has been adopted in cgs units throughout the paper. This is much greater than the maximum brightness temperature for an incoherent emitting source

$$T_{b,\max}^{\text{incoh}} \simeq \Gamma \gamma m_e c^2 / k_B = (5.9 \times 10^{13} \text{ K}) \Gamma_2 \gamma_2, \quad (2)$$

where m_e , c , k are the fundamental constants electron mass, speed of light and Boltzman constant, respectively, Γ is the bulk Lorentz factor of the emitter towards earth (taken as unity if the source is not moving with

a relativistic speed), and $\gamma = \max(\gamma_m, \gamma_a)$ is the characteristic electron Lorentz factor in the emission region, which, for a synchrotron source, is the greater of the minimum injection Lorentz factor γ_m and the Lorentz factor γ_a corresponding to synchrotron self-absorption (Kumar & Zhang 2015). This suggests that FRB emission mechanism must be coherent.

Many coherent radiation mechanisms have been explored to interpret the emission of radio pulsars, which also have the brightness temperature $T_b \gg T_{b,\max}^{\text{incoh}}$ (but is about 10 orders of magnitude lower than that of FRBs). In general, these mechanisms can be grouped into three types (e.g. Melrose 1978): coherent radiation by bunches, intrinsic growth of plasma wave modes, and maser mechanism. The second and third mechanisms were also termed as “plasma maser” and “vacuum maser” mechanisms, respectively. Some of these mechanisms have been reinvented to interpret FRB coherent emission (e.g. Lu & Kumar 2018; Zhang 2020; Xiao et al. 2021; Lyubarsky 2021, for surveys of various mechanisms discussed in the literature).

This paper mainly concerns about the first type of coherent mechanism, namely, coherent radiation by

bunches, also called the “antenna” mechanism. Within this mechanism, charged particles are clustered in both position and momentum spaces and emit as a macroscopic charge. The emission power of the bunch is $P_b \simeq N_{e,b}^2 P_e$, where P_e is the power of individual electrons, and $N_{e,b}$ is the total number of net charges in the bunch. Within the FRB context, a widely discussed possibility is coherent curvature radiation by bunches (Katz 2014; Kumar et al. 2017; Yang & Zhang 2018; Lu & Kumar 2018; Wang et al. 2019; Kumar & Bošnjak 2020; Lu et al. 2020; Yang et al. 2020; Wang & Lai 2020; Cooper & Wijers 2021). Another related mechanism is the so-called “synchrotron maser” mechanism in 90° magnetized relativistic shocks, which in fact invoke cyclotron-radiating bunches of charged particles in momentum space (Lyubarsky 2014; Beloborodov 2017, 2020; Metzger et al. 2019; Plotnikov & Sironi 2019; Margalit et al. 2020). These mechanisms can interpret some FRB emission properties but also suffer from criticisms in theoretical and/or observational aspects (e.g. Zhang 2020; Lyubarsky 2021).

In this paper, we discuss another family of bunching coherent mechanisms, namely, coherent inverse Compton scattering (ICS) by bunches. Before getting into the details of the model, it is informative to clarify the meaning of “bunches” discussed in this paper. In the pulsar literature, “bunches” are usually treated as giant charges surrounded by a background plasma (e.g. Gil et al. 2004). The mechanism was criticized for the formation and maintenance mechanisms of such bunches (e.g. Melrose 1978). Also the surrounding plasma works against the coherence of the bunch and suppresses the coherent emission (Gil et al. 2004; Lyubarsky 2021). For the curvature radiation mechanism widely discussed in the literature, since the radiation power of individual particles is low, highly coherent bunches are required and these criticisms may be relevant (but see Melikidze et al. 2000; Qu & Zhang 2021). However, as will be shown below, in the case of ICS emission, since the emission power of individual particles is much higher, the required coherence for bunches is much reduced. Rather than distinct giant charges surrounded by an ambient medium, the bunches discussed in this paper are merely charge density fluctuations in an relativistic particle outflow (see also Yang & Zhang 2018).

2. COHERENT ICS BY BUNCHES

2.1. General picture

The general picture of the hereby discussed mechanism is the following (Figure 1): Sudden cracking of the crust of a magnetar excites crustal quakes and plasma oscillations near the surface of the magnetar.

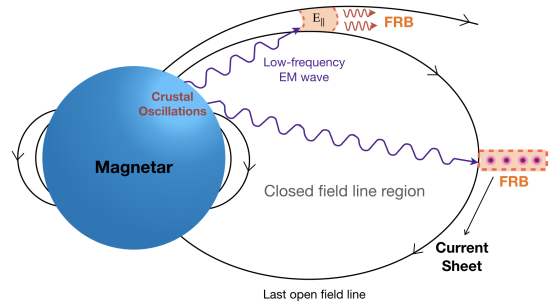


Figure 1. The geometric sketch of the proposed model. Charges in the magnetosphere near the crustal oscillation region send out low-frequency electromagnetic waves which propagate across the closed field line region to reach the emission sites, either in the outer magnetosphere in the open field line region where an E_{\parallel} is developed, or in the current sheet region outside the magnetosphere. Relativistic particles in the emission region upscatter the low-frequency waves and produce FRBs. The FRB emission direction is along the local magnetic field lines in the first scenario and is out of page in the second scenario.

Low-frequency electromagnetic waves with angular frequency ω_0 would be generated by the coherently oscillating charged particles and would propagate across the magnetosphere. The waves encounter bunches of relativistic particles with a typical Lorentz factor γ and a net charge $N_{e,b}e$, which moves along magnetic field lines in the outer magnetosphere or in current sheets outside of the magnetosphere. In the rest-frame of the particle bunch, the incident wave frequency is boosted to $\sim \gamma(1 - \beta \cos \theta_i)\nu_0$. The bunched particles are induced to oscillate at the same frequency in the comoving frame, which is transferred to a lab-frame outgoing ICS frequency

$$\nu \simeq \gamma^2 \nu_0 (1 - \beta \cos \theta_i) = (1 \text{ GHz}) \gamma_{2.5}^2 \nu_{0.4} (1 - \beta \cos \theta_i), \quad (3)$$

where $\nu_0 = \omega_0/2\pi$ and θ_i is the angle between the incident photon momentum and the electron momentum. Similar to curvature radiation, such an ICS mechanism does not depend intrinsically on the dispersive properties of the plasma and may be treated assuming vacuum wave properties. Different from the curvature radiation mechanism which appeals to the curved trajectory of charged particles for acceleration, the ICS mechanism invokes an oscillating electromagnetic field from the low frequency waves to accelerate bunched particles.

Such a mechanism is not new in the pulsar literature. Linear acceleration emission (LAE) invokes an oscillating E_{\parallel} along the direction of particle motion (e.g. Melrose 1978; Rowe 1995). A free-electron laser (FEL) invokes interaction between an electromagnetic disturbance (wiggler) with a relativistically moving bunch

(e.g. Fung & Kuijpers 2004) to power pulsar radio emission or FRB emission Lyutikov (2021a). Lyubarskii (1996) introduced induced upscattering of longitudinal oscillations to interpret pulsar radio emission. Qiao & Lin (1998) considered low-frequency electromagnetic waves generated from regular discharges of an inner vacuum gap in the pulsar polar cap region and showed that ICS off these waves may reproduce many observational features of pulsar radio emission (Qiao et al. 2001; Xu et al. 2000).

2.2. Low frequency waves: generation and propagation

Since FRBs are rarely produced from their sources (e.g. the Galactic magnetar SGR 1935+2154 only produced one detected FRB since its discovery, CHIME/FRB Collaboration et al. 2020; Bochenek et al. 2020, while many X-ray bursts have been produced without association with any FRBs, Lin et al. 2020), it is reasonable to assume that something extraordinary must have happened to trigger an FRB. We envisage the low-frequency electromagnetic waves generated near the surface of the neutron star as one condition to produce FRBs. This may be related to violent oscillations of charged particles near the surface triggered by, e.g. strong oscillations of the neutron star crust during a starquake (e.g. Thompson & Duncan 2001; Beloborodov & Thompson 2007; Wang et al. 2018; Dehman et al. 2020; Yang & Zhang 2021). The bulk of the global oscillation energy would be carried by Alfvén waves that propagate along the magnetic field lines in the form a magnetic pulse, which would deposit energy in the form of particle energy and radiation at a large distance, as envisaged in most of the FRB models (e.g. Kumar & Bošnjak 2020; Lyubarsky 2020; Yuan et al. 2020). However, the same shearing oscillations of the crust would induce oscillations of charges in the near-surface magnetosphere in the direction perpendicular to magnetic field lines, so that a small fraction of the oscillation energy may be radiated by these charges coherently and nearly isotropically as X-mode electromagnetic waves with angular frequency ω_0 , similar to an antenna in a radio station on Earth. Strictly speaking, the electromagnetic waves discussed here are electromagnetic modes propagating in a plasma, which may be equivalent to some forms of fast magnetosonic waves. However, since the magnetization factor σ is extremely high in the inner magnetosphere, the magnetosonic waves all propagate at essentially the speed of light and would behave like electromagnetic waves in vacuum with a proper dispersion relation. Since the electromagnetic waves do not carry the bulk of FRB energy but rather provide seed photons for particles to upscatter at a large radius, the bright-

ness temperature of the low-frequency coherent emission does not need to be very high. In this model, the low frequency waves should at least last several milliseconds (the duration of the FRB), but could last longer (in which case the FRB duration would be defined by the duration of the magnetic pulse dissipation leading to coherent ICS emission by relativistic particles).

For a cold, non-relativistic plasma, the X-mode electromagnetic waves can propagate in the frequency regimes $\omega > \omega_R$, $\omega_L < \omega < \omega_{uh}$, and $\omega < \omega_{lh}$, where ω_R , ω_L are the cutoff frequencies for the R-mode and L-mode and ω_{uh} and ω_{lh} are the upper and lower hybrid principle resonant frequencies, respectively (Boyd & Sanderson 2003). For an electron-positron pair plasma relevant for a pulsar/magnetar magnetosphere, one has $\omega_R = \omega_{uh} = \omega_L = \sqrt{\omega_p^2 + \omega_B^2}$ and $\omega_{lh} = \omega_B$, so that the X-mode electromagnetic waves are free to propagate at $\omega > \sqrt{\omega_p^2 + \omega_B^2}$ or $\omega < \omega_B$ (see Appendix). For a magnetar with surface magnetic field $B_s = 10^{15} \text{ G}$, $B_{s,15}$ and rotation period P , the Goldreich-Julian charge number density (Goldreich & Julian 1969; Ruderman & Sutherland 1975) is

$$n_{\text{GJ}} \simeq \frac{\Omega B}{2\pi c e} \simeq (6.9 \times 10^7 \text{ cm}^{-3}) B_{s,15} P^{-1} \hat{r}_2^{-3}, \quad (4)$$

where $\Omega = 2\pi/P$ is the angular frequency, and

$$\hat{r} \equiv \frac{r}{R} \quad (5)$$

is the radius r normalized to the neutron star radius $R = 10^6 \text{ cm}$, R_6 . The plasma number density can be estimated as

$$n = \xi n_{\text{GJ}}, \quad (6)$$

where ξ is the multiplicity parameter due to electron-positron pair production. As a result, the plasma frequency and the Larmor frequency can be estimated as

$$\begin{aligned} \omega_p &= \left(\frac{4\pi n e^2}{m_e} \right)^{1/2} \\ &\simeq (4.7 \times 10^8 \text{ rad s}^{-1}) \xi^{1/2} B_{s,15}^{1/2} P^{-1/2} \hat{r}_2^{-3/2} \end{aligned} \quad (7)$$

$$\omega_B = \frac{eB}{m_e c} \simeq (1.8 \times 10^{16} \text{ rad s}^{-1}) B_{s,15} \hat{r}_2^{-3}. \quad (8)$$

It is also informative to evaluate these frequencies at the light cylinder of the magnetar, which has $r = R_{\text{lc}} = c/\Omega$ and

$$\hat{r}_{\text{lc}} = (4.8 \times 10^3) P R_6^{-1}. \quad (9)$$

This gives

$$\omega_p^{\text{lc}} \simeq (1.4 \times 10^6 \text{ rad s}^{-1}) \xi^{1/2} B_{s,15}^{1/2} P^{-2} R_6^{3/2} \quad (10)$$

$$\omega_B^{\text{lc}} \simeq (1.6 \times 10^{11} \text{ rad s}^{-1}) B_{s,15} P^{-3} R_6^3. \quad (11)$$

One can see that for the low-frequency EM waves we are interested in, the condition $\omega_0 \ll \omega_p \ll \omega_B$ is satisfied throughout the magnetosphere. Therefore the X-mode low frequency waves are transparent to the magnetosphere in all directions for essentially all frequencies (see also [Lu et al. 2019](#)).

The above treatment makes the assumption of a cold plasma. Near surface electromagnetic waves need to penetrate through the closed field line region to reach the emission sites in our two scenarios (Fig.1). Since the closed field line region of a magnetar is likely populated with inactive non-relativistic particles, the cold plasma dispersion relation treatment can serve the purpose for our discussion. We note that the dispersion relation is more complicated when relativistic plasmas are considered (e.g. [Arons & Barnard 1986](#); [Lyubarskii & Petrova 1998](#); [Melrose 2017](#)). Nonetheless, the conclusion that X-mode low-frequency electromagnetic waves are transparent in a magnetar magnetosphere remains valid for such more complicated situations.

2.3. Cross section and ICS power

In the following, we perform a vacuum treatment of the ICS process for simplicity. A more rigorous treatment should consider various plasma effects (e.g. [Melrose 1978](#); [Rowe 1995](#); [Lyubarskii 1996](#); [Fung & Kuijpers 2004](#); [Lyutikov 2021a](#)). However, a vacuum treatment can catch the essential features of this family of models, as discussed below.

The Compton scattering (in the rest frame of electron) cross section in a strong magnetic field is significantly modified from the Thomson cross section σ_T . The cross section for the two modes of photons read ([Herold 1979](#); [Xia et al. 1985](#))

$$\begin{aligned} \sigma'(1) &= \sigma_T \left\{ \sin^2 \theta'_i + \frac{1}{2} \cos^2 \theta'_i \left[\frac{\omega'^2}{(\omega' + \omega_B)^2} + \frac{\omega'^2}{(\omega' - \omega_B)^2} \right] \right\} \\ \sigma'(2) &= \frac{\sigma_T}{2} \left[\frac{\omega'^2}{(\omega' + \omega_B)^2} + \frac{\omega'^2}{(\omega' - \omega_B)^2} \right]. \end{aligned} \quad (13)$$

where 1 denotes the mode that the electric vector \mathbf{E}' of the incident wave is parallel to the (\mathbf{k}, \mathbf{B}) plane, and 2 denotes the mode that \mathbf{E}' is perpendicular to the plane. Here the primed symbols denote in the rest frame of the electron (since electrons move along magnetic field lines, ω_B does not change when the frame changes). In this frame, the photon incident angle θ'_i is connected to the lab-frame incident angle θ_i through

$$\sin \theta'_i = \frac{\sin \theta_i}{\gamma(1 - \beta \cos \theta_i)}, \quad (14)$$

$$\cos \theta'_i = \frac{\cos \theta_i - \beta}{1 - \beta \cos \theta_i}, \quad (15)$$

where γ and β are the Lorentz factor and dimensionless speed of the electron, respectively. In the lab frame, the ICS cross section is related to the the rest-frame Compton scattering cross section through $\sigma = (1 - \beta \cos \theta_i) \sigma'$ ([Pacholczyk 1970](#)). This finally gives

$$\begin{aligned} \sigma(1) &= \sigma_T \left\{ \frac{\sin^2 \theta_i}{\gamma^2(1 - \beta \cos \theta_i)} + \frac{(\cos \theta_i - \beta)^2}{2(1 - \beta \cos \theta_i)} \right. \\ &\quad \times \left. \left[\frac{\omega'^2}{(\omega' + \omega_B)^2} + \frac{\omega'^2}{(\omega' - \omega_B)^2} \right] \right\}, \end{aligned} \quad (16)$$

$$\sigma(2) = \frac{\sigma_T}{2} \left[\frac{\omega'^2}{(\omega' + \omega_B)^2} + \frac{\omega'^2}{(\omega' - \omega_B)^2} \right]. \quad (17)$$

At this point, it is informative to compare the order of magnitude of the two terms in the curly brackets. In the lab frame, θ_i can be an arbitrary angle, so that all the factors involving θ_i could be of the order of unity. For our nominal parameters $\gamma \sim 10^{2.5}$ and $\omega_0 \sim (2\pi)10^4$ and noticing $\omega' \simeq \gamma\omega_0(1 - \beta \cos \theta_i)$, the first term in $\sigma(1)$ is therefore $\propto \gamma^{-2} \sim 10^{-5}$ and the second term (also $\sigma(2)$) is $\propto (\omega'/\omega_B)^2 \sim (10^6/10^{11})^2 \sim 10^{-10}$ even at the light cylinder where ω_B is the lowest in the magnetosphere. One can therefore ignore $\sigma(2)$ and the second term of $\sigma(1)$, so that only (see also [Qiao & Lin 1998](#))

$$\sigma(1) \simeq \sigma_T \frac{\sin^2 \theta_i}{\gamma^2(1 - \beta \cos \theta_i)} \simeq (6.65 \times 10^{-30} \text{ cm}^2) \gamma_{2.5}^{-2} f(\theta_i) \quad (18)$$

is relevant, where $f(\theta_i) = \sin^2 \theta_i / (1 - \beta \cos \theta_i)$ is defined.

The ICS emission power of a single relativistic electron may be estimated as

$$\begin{aligned} P_e^{\text{ICS}} &\simeq \frac{4}{3} \gamma^2 \sigma(1) c U_{\text{ph}} \\ &\simeq (2.1 \times 10^{-7} \text{ erg s}^{-1}) f(\theta_i) (\delta B_{0,6})^2 \hat{r}_2^{-2}, \end{aligned} \quad (19)$$

where

$$\begin{aligned} U_{\text{ph}} &\simeq \frac{(|\delta \mathbf{E}_0 \times \delta \mathbf{B}_0|)^2}{4\pi} \hat{r}_2^{-2} \\ &\simeq (8.0 \times 10^6 \text{ erg cm}^{-3}) (\delta B_{0,6})^2 \hat{r}_2^{-2} \end{aligned} \quad (20)$$

is the photon energy density in the emission region, and $\delta \mathbf{E}_0$ and $\delta \mathbf{B}_0$ are the electric and magnetic vectors of the low frequency waves near the surface region, which we normalize to a relatively small value $\delta B_0 \sim 10^6 \text{ G}$. Comparing with the curvature radiation (CR) emission power of a single electron

$$P_e^{\text{CR}} = \gamma^4 \frac{2e^2 c}{3\rho^2} \simeq (4.6 \times 10^{-15} \text{ erg s}^{-1}) \gamma_{2.5}^4 \rho_8^{-2}, \quad (21)$$

one can see that the ICS power is much larger, i.e. $P_e^{\text{ICS}} \gg P_e^{\text{CR}}$, a known fact in pulsar studies ([Qiao & Lin 1998](#); [Zhang et al. 1999](#)). This suggests that when coherent ICS operates, the effect of coherent CR is negligibly small.

2.4. Coherent ICS emission by bunches

A bunch of leptons with a net charge value of $N_{e,b}e$ can radiate coherently in response to the low frequency waves, with an emitted power of $\sim N_{e,b}^2 P_e^{\text{ICS}}$. The observed power is boosted by a factor of γ^2 because the observer time is shorter by a factor of $(1 - \beta \cos \theta) \sim 1/\gamma^2$ (when the angle between the charge motion direction and the line of sight is $\theta < 1/\gamma$) with respect to the emission time. For a total number of bunch number N_b , the total luminosity of the emitter may be written as

$$L \simeq N_b N_{e,b}^2 P_e^{\text{ICS}} \gamma^2. \quad (22)$$

One may estimate

$$N_{e,b} = \zeta n_{\text{GJ}} A_b \lambda, \quad (23)$$

where A_b is the cross section of the bunch, $\lambda = c/\nu$ is the wavelength, and ζ is the factor to denote the net charge density with respect to n_{GJ} . The most conservative estimate is (Kumar et al. 2017)

$$A_b^{\text{min}} = \pi(\gamma\lambda)^2, \quad (24)$$

since it describes the causally connected area of a relativistic bunch¹. Since the ICS mechanism is very efficient, in the following we use this conservative limit. Plugging Eqs. (4), (19), (23), and (24) in Eq. (22), one finally gets

$$L \simeq (7.3 \times 10^{38} \text{ erg s}^{-1}) \zeta^2 N_{b,5} \gamma_{2.5}^6 \nu_9^{-6} \times B_{s,15}^2 P^{-2} f(\theta_i) \delta B_{0,6}^2 \hat{r}_2^{-8}. \quad (25)$$

One may compare Eq.(25) with the true FRB luminosity from the observations, i.e. $L^{\text{obs}} = L_{\text{iso}}^{\text{obs}} \max(\pi/\gamma^2, \pi\theta_j^2)$, where θ_j is the half opening angle of the FRB jet. For the narrow jet scenario with solid angle defined by the γ^{-1} cone, one has $L^{\text{obs}} \simeq (3 \times 10^{38} \text{ erg s}^{-1}) L_{\text{iso},43}^{\text{obs}} \gamma_{2.5}^{-2}$. One can see that the coherent ICS mechanism can easily account for the typical FRB luminosity by only requiring a moderate number of $N_b \sim 10^5$ even with the most conservative estimate of the coherent bunch cross section A_b^{min} . From Eq.(22), one can immediately see that the required $N_b N_{e,b}^2$ for the coherent ICS model is smaller by a factor $P_e^{\text{CR}}/P_e^{\text{ICS}} \sim 2.2 \times 10^{-8}$ to interpret the same FRB luminosity for the same electron Lorentz factor γ .

A bunch with $N_{e,b}$ particles cools more efficiently than single particles since the emission power is $\sim N_{e,b}^2$ times of the individual particle emission power. The bunch

quickly loses the total energy, which itself is not large enough to power FRB emission. In order to power FRB emission, a sustained E_{\parallel} is needed to continuously pump energy to the bunch. Such a scenario is relevant to coherent CR by bunches (Kumar et al. 2017). Below we investigate the case for coherent ICS emission. The cooling timescale of the coherent ICS bunches may be estimated as

$$t_{c,b} = \frac{N_{e,b} \gamma m_e c^2}{N_{e,b}^2 P_e^{\text{ICS}}} \simeq (2.1 \times 10^{-15} \text{ s}) \times \zeta^{-1} \nu_9^3 \gamma_{2.5}^{-1} B_{s,15}^{-1} P[f(\theta_i)]^{-1} \delta B_{0,6}^{-2} \hat{r}_2^5. \quad (26)$$

Since this is much shorter than the typical FRB duration, similar to the bunched coherent CR mechanism, a parallel electric field is also needed to continuously pump energy to the bunch. One may estimate the strength of this E_{\parallel} by requiring $N_{e,b} e (ct_{c,b}) \simeq N_{e,b} \gamma m_e c^2$, which gives

$$E_{\parallel} \simeq \frac{N_{e,b} P_e^{\text{ICS}}}{ec} \simeq (8.6 \times 10^9 \text{ esu}) \times \zeta \nu_9^{-3} \gamma_{2.5}^2 B_{s,15} P^{-1} f(\theta_i) \delta B_{0,6}^2 \hat{r}_2^{-5}. \quad (27)$$

This is larger than that required for the bunched coherent CR mechanism because of a larger P_e . However, in view of the steep dependence on \hat{r} , the required E_{\parallel} comfortably falls into the range available for magnetars if \hat{r} is somewhat greater than 100. Several mechanisms may provide this E_{\parallel} at $\hat{r} \gg 1$. First, a slot gap near the last open field line region may extend from the neutron surface all the way to light cylinder because the region cannot be filled with electron-positron pairs produced from a pair production cascade – a consequence of straight line propagation of γ -rays and curved magnetic field lines (e.g. Arons & Scharlemann 1979; Muslimov & Harding 2004). Charge starvation may become more prominent in old, low-twist magnetars (Wadiasingh et al. 2020). Second, Alfvén waves propagating along magnetic field lines would enter a charge starved region at a large enough radius because the charge density may become insufficient to provide the required current (e.g. Kumar & Bošnjak 2020; Lu et al. 2020, cf. Chen et al. 2020). Third, in the current sheet outside of the magnetosphere, an E_{\parallel} naturally exists in the magnetic reconnection layer (e.g. Lyubarsky 2020; Kalapotharakos et al. 2018; Philippov & Spitkovsky 2018).

3. SALIENT FEATURES OF THE MODEL

3.1. Two physical scenarios

After discussing some general properties of this model, we discuss two specific scenarios within the framework

¹ The true A_b can be in principle much larger, up to the area defined by the Fresnel radius i.e. $A_b \simeq \pi x \lambda$, where x is the distance between the emission site and the projected focus of the tangential lines of the emission region field lines.

of the magnetar repeating FRB models. The geometric configurations of the two scenarios are presented in Figure 1.

The first scenario is similar to that of Kumar & Bošnjak (2020) and Lu et al. (2020), but with coherent curvature radiation by bunches replaced by the more efficient coherent ICS by bunches. Within this scenario, neutron star crust cracking excites crustal seismic waves, which in turn excite Alfvén waves in the magnetosphere. Low frequency electromagnetic waves (effectively fast magnetosonic waves in a high- σ medium) are generated and the X-mode waves propagate with a speed close to the speed of light. The waves are up-scattered at a large enough altitude where E_{\parallel} is developed, either due to charge starvation in the Alfvén waves (Kumar & Bošnjak 2020) or a due to the traditional pulsar gap mechanism (Arons & Scharlemann 1979; Cheng et al. 1986; Muslimov & Harding 2004; Wadiasingh et al. 2020). Assuming that this emission site is at $\hat{r} \sim 100$, based on the scalings presented in Section 2.3, the FRB luminosities are easily interpreted even if the low frequency waves have a relatively low amplitude with $\delta B_0 \sim 10^6$ G.

In the second scenario, the emission site is in the reconnection current sheet region just outside of the light cylinder, similar to Lyubarsky (2020). However, the radiation mechanism is via coherent ICS by bunches rather than oscillations of colliding magnetic islands within the current sheet as proposed by Lyubarsky (2020). Here the bunches could be density fluctuations in the turbulent relativistic particle outflows within the reconnection layer. At this radius, the amplitude of low frequency waves is degraded significantly with respect to that in the near-surface region. Since magnetic reconnection is enhanced by a strong magnetic pulse that is eventually responsible for the FRB, the magnetic energy density is enhanced by a factor of $b \equiv B_{\text{pulse}}/B_{\text{wind}}$ in the current sheet region (Lyubarsky 2020). Based on magnetic flux conservation, the cross section of the magnetic tube is also compressed by the same factor b . Since the length scale in the \mathbf{B} direction is not changed, this leads to a local plasma density increased by a factor of $\sim b$. According to Eqs.(1) and (4) of Lyubarsky (2020), one estimates $b \sim 4 \times 10^4$. As a result, we can estimate the local charge density using Eq.(6) with $\hat{r} = \hat{r}_{\text{lc}}$ (Eq.(9)) and $\zeta \simeq b = 4 \times 10^4 b_{4.6}$. Rewriting the equations presented in Section 2.3 with $\hat{r} = \hat{r}_{\text{lc}}$ (Eq.(9)), one obtains:

$$U_{\text{ph}}^{\text{lc}} \simeq (3.5 \times 10^3 \text{ erg cm}^{-3}) \delta B_{0,6}^2 P^{-2} R_6^2 \quad (28)$$

$$P_e^{\text{ICS,lc}} \simeq (9.3 \times 10^{-11} \text{ erg s}^{-1}) \delta B_{0,6}^2 P^{-2} f(\theta_i) R_6^2 \quad (29)$$

$$L^{\text{lc}} \simeq (4.4 \times 10^{38} \text{ erg s}^{-1}) b_{4.6}^2 N_{b,9} \gamma_{2.5}^6 \nu_9^{-6} \times B_{s,15}^2 P^{-10} f(\theta_i) \delta B_{0,6}^2 R_6^8 \quad (30)$$

$$t_{c,b}^{\text{lc}} \simeq (1.3 \times 10^{-11} \text{ s}) b_{4.6}^{-1} \nu_9^3 \gamma_{2.5}^{-1} B_{s,15}^{-1} \times P^6 [f(\theta_i)]^{-1} \delta B_{0,6}^{-2} R_6^{-5} \quad (31)$$

$$E_{\parallel}^{\text{lc}} \simeq (1.4 \times 10^6 \text{ esu}) b_{4.6} \nu_9^{-3} \gamma_{2.5}^2 B_{s,15} P^{-6} f(\theta_i) \delta B_{0,6}^2 R_6^5. \quad (32)$$

One can see that the FRB luminosities can be still explained with $\delta B_0 \sim 10^6$ G but a somewhat larger bunch number $N_b \sim 10^9$.

Note that in the magnetic reconnection site, the reconnection-driven electric field is perpendicular to \mathbf{B} . This is different from the first scenario where E_{\parallel} is along the \mathbf{B} field direction. However, since we do not know the geometric configuration of the FRB central engine, the same FRB may be interpreted by the two scenarios with different viewing geometries: The inner magnetospheric scenario has the viewing angle sweep the open field line region, whereas the reconnection scenario has the viewing angle sweep the equatorial plane (see Fig. 1).

3.2. Energy budget

In our model, the energy budget to power FRBs is carried by particles rather than by low frequency waves. The latter only carries a small amount of energy. Its role is to provide seed photons for coherent ICS emission to operate. Since $\delta B \propto r^{-1}$ and $B \propto r^{-3}$, with the nominal parameters $\delta B_0 \sim 10^6$ G and $B_s \sim 10^{15}$ G, one estimates $\delta B^{\text{lc}}/B^{\text{lc}} = 4.8 \times 10^{-6} P R_6^{-1} \ll 1$ at the light cylinder. As a result, the enhancement of the magnetospheric Thomson cross section (which is relevant when $\delta B > B$, Beloborodov 2021)² does not occur for the low-frequency waves so that they can propagate freely within the magnetar magnetosphere³. The energy of the emitting particles comes from the main magnetic pulse driven by the violent event itself. The energy that powers the FRB is first carried by the Alfvén waves, which advect particles to a large altitude where an E_{\parallel} is developed in a charge-starved region in the magnetar magnetosphere (Kumar & Bošnjak 2020; Muslimov & Harding 2004; Wadiasingh et al. 2020) or in magnetic

² In a weak background \mathbf{B} field, the Thomson scattering cross section is enlarged by a factor of a^2 for strong waves for $a \gg 1$, where a is the amplitude parameter (Yang & Zhang 2020). However, with the presence of a strong background field, this effect is suppressed until the wave vector δB becomes stronger than the background B .

³ The constraint on the upscattered waves still applies, especially if the emission has a very high luminosity (Beloborodov 2021). The problem is alleviated if the emission altitude is high (as envisaged in our scenarios) and when radiation pressure (Ioka 2020; Wang et al. 2021) or ponderomotive pre-acceleration of background plasma (Lyutikov 2021b) by the intense FRB emission field are considered.

reconnection sites in the current sheet just outside the magnetosphere (Lyubarsky 2020; Kalapotharakos et al. 2018; Philippov & Spitkovsky 2018). Particles are accelerated in these E_{\parallel} fields so that their ultimate energy comes from the magnetic pulse itself.

3.3. Polarization properties

Since only the X-mode low frequency waves can propagate in the magnetosphere, the incident photon is linearly polarized and has an electric field vector perpendicular to the local magnetic field direction. The outgoing photon in an ICS process is also linearly polarized. According to Herold (1979), only the cross section from mode 1 to mode 1 is related to the $\sin^2 \theta_i$ term in Eq.(17). All the other scattering modes (1 to 2, 2 to 1, 2 to 2) involve the $[\omega'^2/(\omega' + \omega_B)^2 + \omega'^2/(\omega' - \omega_B)^2]$ term, which is negligibly small for our problem. The 1 mode has both an X-mode component and an O-mode component. The latter cannot propagate. As a result, our model predicts linearly polarized X-mode emission with a $\sim 100\%$ degree of linear polarization in the X mode. Circular polarization may develop under special conditions (Xu et al. 2000). This is in general consistent with the FRB observations (e.g. Gajjar et al. 2018; Michilli et al. 2018; Cho et al. 2020; Day et al. 2020; Luo et al. 2020).

The duration of an FRB is defined by the longer of the emission duration and the timescale for the line-of-sight to sweep the bundle of the magnetic field lines where emitting particles flow out (Wang et al. 2019, 2021). For a slow rotator and an emission site far from the neutron star surface, the polarization angle would be nearly constant across an individual burst, as observed in some repeating FRBs (e.g. Michilli et al. 2018). For a rapid rotator and an emission site closer to the neutron star surface, the polarization angle may display diverse swing features, as observed in some other repeating FRBs (Luo et al. 2020). Our model can account for both patterns.

3.4. Narrow spectrum and frequency down-drifting

The characteristic frequency of coherent ICS emission Eq.(3) depends on ω_0 , γ and θ_i . For the coherent mechanism to work, particles need to continuously tap energy from E_{\parallel} so that they are likely emitting in the radiation-reaction-limited regime. As a result, γ may remain roughly constant during the emission phase. At the large emission radius as envisaged in the two scenarios, θ_i varies little as the line of sight sweeps across different field lines. For a seismic oscillation originating from the neutron star crust, the oscillation frequency ω_0 depends on the resonance frequency of the crust which may have a characteristic value. As a result, the characteristic frequency ν has a narrow value range, unlike

curvature radiation which is an intrinsically broad band mechanism (Yang & Zhang 2018)⁴. This is consistent with the narrow-band emission as observed from repeating FRBs (Spitler et al. 2016; CHIME/FRB Collaboration et al. 2021).

The characteristic Lorentz factor of electrons may slightly decrease with radius. If so, the outgoing ICS frequency would decrease with radius and give a radius-to-frequency mapping within the ICS model (Qiao & Lin 1998). Alternatively, as the seismic waves damp, ω_0 would gradually decrease with a decreasing amplitude. This would also result in a decreasing ν of FRB emission with reduced amplitude. Both factors may offer an explanation to the observed sub-pulse frequency down-drifting pattern (also called the “sad trombone” effect) (Hessels et al. 2019; CHIME/FRB Collaboration et al. 2019a,b)⁵.

3.5. Required degree of coherence

Since the ICS emission power of individual electrons is much higher than that of curvature radiation, the required degree of coherence in the bunch is much lower. In the scalings presented in Section 2.3, the net charge parameter ζ is normalized to unity. In other words, a bunch with the Goldreich-Julian net charge density can produce the high brightness temperature of FRB emission. In fact, the model even allows the bunch charge density to be below the Goldreich-Julian density, with the luminosity compensated with a somewhat larger total number of bunches, N_b , which is currently normalized to a small value. The only requirement to make a bunch is that there are fluctuations of net charge density in space with respect to the background number density (Yang & Zhang 2018). This alleviates traditional criticisms on the bunching mechanisms within the context of curvature radiation regarding the formation and maintenance of bunches (Melrose 1978). Since the mechanism can apply to magnetospheres with a low plasma density (see also Wadiasingh et al. 2020), another major criticism on the bunching mechanism, i.e. the suppression of coherent emission flux due to the dense plasma effect (Gil et al. 2004; Lyubarsky 2021), is also alleviated.

4. CONCLUSIONS AND DISCUSSION

We have proposed a new family of FRB emission model invoking coherent ICS emission by bunches within

⁴ A relatively narrow spectrum can be obtained if oppositely charged particles are spatially separated (Yang et al. 2020).

⁵ Other interpretations include radius-to-frequency mapping for curvature radiation (Wang et al. 2019), decreasing magnetic field strengths in synchrotron maser shocks (Metzger et al. 2019), or external free-free absorption (Kundu & Zhang 2021).

or just outside of the magnetosphere of a flaring magnetar. The key assumption is that the oscillations of the magnetar crust would excite oscillations of charges in the magnetosphere near the neutron star surface, which would excite low-frequency electromagnetic waves with an antenna mechanism. The X-mode of these waves could propagate freely in the magnetosphere. Bunched relativistic particles in the outer magnetosphere or in the current sheet region outside of the magnetosphere could upscatter the low frequency waves coherently to power FRBs observed in the \sim GHz band (Eq.(3)). For standard parameters, the ICS power of individual particles (Eq.(19)) is much greater than that of curvature radiation (Eq.(21)). As a result, the typical FRB luminosity can be easily reproduced with a low charge density bunch (plasma density of the order of or even lower than the Goldreich-Julian charge density) and a moderate number of bunches (Eqs.(25) and (30)). An E_{\parallel} is needed to sustain the coherent radiation (similar to the curvature radiation mechanism), but such an E_{\parallel} is expected in charge starved region in the outer magnetar magnetosphere or in the current sheet outside the magnetosphere. This model can account for several observational properties of repeating FRBs, including nearly 100% polarization degree of emission, constant or varying polarization angle across each burst, narrow emission spectrum, and frequency downdrifting. The low degree of coherence also alleviates several criticisms to

the bunched coherent curvature radiation mechanism, including the formation and maintenance of bunches as well as the plasma suppression effect.

The vacuum treatment discussed in this paper shares some essential features with a broader family of models that invoke relativistic particles scattering off various plasma waves. For example, Lyubarskii (1996) presented a detailed treatment of induced scattering of relativistic particles off longitudinal subluminal plasma waves and showed that superluminal transverse electromagnetic waves can be efficiently generated to power pulsar radio emission with the characteristic radius-to-frequency mapping. Lyutikov (2021a) studied the scattering of relativistic particles off Alfvén wave wigglers and showed a narrow characteristic frequency and a high efficiency, similar to the features of the vacuum model presented in this paper. All these suggest that ICS of relativistic particles against various forms of low-frequency waves could be in general an attractive mechanism to power magnetospheric FRB emission from magnetars.

The author acknowledges the referee for critical comments that helped to improve the presentation of the paper, Yuan-Pei Yang, Pawan Kumar, and Wenbin Lu for excellent comments, Guojun Qiao for discussion and encouragement, and Yuanhong Qu for discussion and the help to draw the figure.

APPENDIX

A. PROPAGATION OF LOW FREQUENCY WAVES IN A MAGNETAR MAGNETOSPHERE

The low frequency electromagnetic waves conjectured in this paper need to propagate through the closed field line region of the magnetar to reach the two FRB emission regions (Fig. 1). Since the particles residing in the closed field line region of a magnetar magnetosphere are believed to have non-relativistic motion, the dispersion relation of wave propagation may be treated under the assumption of a cold plasma. For a cold, magnetized medium, the conductivity is a tensor σ_{ij} so that $\mathbf{j} = \sigma_{ij} \cdot \mathbf{E}$, where \mathbf{E} is the electric field vector of the wave. Define the dielectric tensor

$$\epsilon_{ij} = \delta_{ij} + 4\pi i \sigma_{ij} / \omega, \quad (\text{A1})$$

where ω is the angular frequency of a wave. The fourth Maxwell's equation becomes $\mathbf{n} \times (\mathbf{n} \times \mathbf{E}) = -\epsilon_{ij} \cdot \mathbf{E}$, which defines the dispersion relations for wave propagation. In general, defining θ as the angle between the wave number vector \mathbf{k} and the magnetic field vector \mathbf{B} , one can write the Maxwell response tensor as (e.g. Boyd & Sanderson 2003)

$$\epsilon_{ij} \equiv \begin{pmatrix} S - n^2 \cos^2 \theta & -iD & n^2 \cos \theta \sin \theta \\ iD & S - n^2 & 0 \\ n^2 \cos \theta \sin \theta & 0 & P - n^2 \sin^2 \theta \end{pmatrix} \quad (\text{A2})$$

where \mathbf{B} is defined in the $\hat{\mathbf{z}}$ direction. Here

$$S = \frac{1}{2}(R + L) = 1 - \frac{\omega_p^2(\omega^2 + \Omega_i \Omega_e)}{(\omega^2 - \Omega_i^2)(\omega^2 - \Omega_e^2)}, \quad (\text{A3})$$

$$D = \frac{1}{2}(R - L) = \frac{\omega_p^2 \omega (\Omega_i + \Omega_e)}{(\omega^2 - \Omega_i^2)(\omega^2 - \Omega_e^2)}, \quad (\text{A4})$$

$$R = 1 - \frac{\omega_p^2}{(\omega + \Omega_i)(\omega + \Omega_e)}, \quad (\text{A5})$$

$$L = 1 - \frac{\omega_p^2}{(\omega - \Omega_i)(\omega - \Omega_e)}, \quad (\text{A6})$$

$$P = 1 - \frac{\omega_p^2}{\omega^2}, \quad (\text{A7})$$

where ω_p is the plasma frequency, $\Omega_e = q_e B/m_e c = -eB/m_e c = -\omega_B$ is the electron gyration frequency (which is the Larmor frequency ω_B with a negative sign), and $\Omega_i = q_i B/m_i c$ is the ion gyration frequency (positive sign). For an ion with atomic number Z and mass number A , one has $\Omega_i = ZeB/Am_p c \ll \omega_B$. For hydrogen, one has $\Omega_i = eB/m_p c$. For an electron positron plasma, one has $\Omega_i = eB/m_e c = -\Omega_e = \omega_B$. The general dispersion relation for cold plasma waves is

$$An^4 - Bn^2 + C = 0, \quad (\text{A8})$$

where

$$A = S \sin^2 \theta + P \cos^2 \theta, \quad (\text{A9})$$

$$B = RL \sin^2 \theta + PS(1 + \cos^2 \theta) \quad (\text{A10})$$

$$C = PRL. \quad (\text{A11})$$

The propagation of the waves is prohibited at $k = 0$ (cut-offs) or at $k \rightarrow \infty$ (resonances) for certain propagation angles. At principle resonances ($k \rightarrow \infty$ and $\theta_{\text{res}} = 0$ or 90° , where the resonant angle θ_{res} is defined by $\tan^2 \theta_{\text{res}} = -P/S$), propagation in all directions is prohibited.

For the case of electromagnetic waves propagating along a magnetic field line, i.e. $\mathbf{k} \parallel \mathbf{B}$, the dispersion relations become $n^2 = R$ and $n^2 = L$. Making $R = 0$ and $L = 0$, one can define two cut-off frequencies for the R-mode and L-mode, respectively, i.e.

$$\omega_R \equiv \left[\omega_p^2 + \frac{(\Omega_i - \Omega_e)^2}{4} \right]^{1/2} - \frac{(\Omega_i + \Omega_e)}{2} = \sqrt{\omega_p^2 + \omega_B^2}, \quad (\text{A12})$$

$$\omega_L \equiv \left[\omega_p^2 + \frac{(\Omega_i - \Omega_e)^2}{4} \right]^{1/2} + \frac{(\Omega_i + \Omega_e)}{2} = \sqrt{\omega_p^2 + \omega_B^2}. \quad (\text{A13})$$

Hereafter the second equation in each expression is for a pair plasma, where $\Omega_i = -\Omega_e = \omega_B$ is adopted. The principle resonances can be obtained from $R \rightarrow \infty$ and $L \rightarrow \infty$, which gives

$$\omega_{\text{res,R}} = -\Omega_e = \omega_B, \quad (\text{A14})$$

$$\omega_{\text{res,L}} = \Omega_i = \omega_B. \quad (\text{A15})$$

Electromagnetic waves are transparent above the cut-off frequencies or below the resonances. So for $\mathbf{k} \parallel \mathbf{B}$, the condition for wave propagation in a cold, magnetized plasma is

$$\omega > \sqrt{\omega_p^2 + \omega_B^2}, \quad \text{or} \quad \omega < \omega_B. \quad (\text{A16})$$

For the case of electromagnetic waves propagating in the direction perpendicular to the field lines, i.e. $\mathbf{k} \perp \mathbf{B}$, one should consider two modes: the O-mode with $\mathbf{E} \parallel \mathbf{B}$ and the X-mode with $\mathbf{E} \perp \mathbf{B}$. The O-mode is similar to the case as if no magnetic field exists (the electron moving in response of the \mathbf{E} field does not feel the Lorentz force from \mathbf{B}). Its cut-off frequency is defined by $P = 0$, i.e. $\omega = \omega_p$. The waves cannot propagate at $\omega < \omega_p$.

The X-mode propagation is more complicated. Taking $\theta = 90^\circ$, the dispersion equation (Eq.(A8)) is simplified to

$$n^2 = \frac{RL}{S}. \quad (\text{A17})$$

The cut-off frequencies are again defined by $R = 0$ (i.e. $\omega = \omega_R$) and $L = 0$ (i.e. $\omega = \omega_L$), and the resonance is defined by $S = 0$, with the principle resonances defined with an additional condition $\theta_{\text{res}} = \pi/2$. This demands

$\omega^4 - \omega^2(\omega_p^2 + \Omega_i^2 + \Omega_e^2) - \Omega_i\Omega_e(\omega^2 - \Omega_i\Omega_e) = 0$, which defines two principle resonances

$$\omega^2 = \left(\frac{\omega_p^2 + \Omega_i^2 + \Omega_e^2}{2} \right) \left[1 \pm \left(1 + \frac{4\Omega_i\Omega_e(\omega_p^2 - \Omega_i\Omega_e)}{(\omega_p^2 + \Omega_i^2 + \Omega_e^2)^2} \right)^{1/2} \right]. \quad (\text{A18})$$

For a pair plasma ($\Omega_i = -\Omega_e = \omega_B$), one obtains the two (upper and lower) hybrid resonances as

$$\omega_{\text{uh}}^2 = \omega_p^2 + \omega_B^2, \quad (\text{A19})$$

$$\omega_{\text{lh}}^2 = \omega_B^2. \quad (\text{A20})$$

The cut-off bands for X-mode in the case of $\mathbf{k} \perp \mathbf{B}$ is $\omega_{\text{uh}} < \omega < \omega_R$ and $\omega_{\text{lh}} < \omega < \omega_L$. As shown above, for a pair plasma, one has $\omega_R = \omega_{\text{uh}} = \omega_L = \sqrt{\omega_p^2 + \omega_B^2}$ and $\omega_{\text{lh}} = \omega_B$. One therefore draws the conclusion that the cut-off band for a pair plasma in $\mathbf{k} \perp \mathbf{B}$ X mode is identical to Eq.(A16) derived for the $\mathbf{k} \parallel \mathbf{B}$ case.

Since both $\theta = 0$ and $\theta = 90^\circ$ cases (the latter for X-mode only) have the identical wave propagation condition, Eq.(A16) should apply to the oblique case with an arbitrary θ value for the X-mode waves. O-mode waves cannot propagate below ω_p .

REFERENCES

- Arons, J., & Barnard, J. J. 1986, ApJ, 302, 120
Arons, J., & Scharlemann, E. T. 1979, ApJ, 231, 854
Beloborodov, A. M. 2017, ApJL, 843, L26
—, 2020, ApJ, 896, 142
—, 2021, arXiv e-prints, arXiv:2108.07881
Beloborodov, A. M., & Thompson, C. 2007, ApJ, 657, 967
Bochenek, C. D., Ravi, V., Belov, K. V., et al. 2020, Nature, 587, 59
Boyd, T. J. M., & Sanderson, J. J. 2003, The Physics of Plasmas
Chen, A. Y., Yuan, Y., Beloborodov, A. M., & Li, X. 2020, arXiv:2010.15619
Cheng, K. S., Ho, C., & Ruderman, M. 1986, ApJ, 300, 522
CHIME/FRB Collaboration, Amiri, M., Bandura, K., et al. 2019a, Nature, 566, 235
CHIME/FRB Collaboration, Andersen, B. C., Bandura, K., et al. 2019b, ApJL, 885, L24
CHIME/FRB Collaboration, Andersen, B. C., Bandura, K. M., et al. 2020, Nature, 587, 54
CHIME/FRB Collaboration, :, Amiri, M., et al. 2021, arXiv e-prints, arXiv:2106.04352
Cho, H., Macquart, J.-P., Shannon, R. M., et al. 2020, ApJL, 891, L38
Cooper, A. J., & Wijers, R. A. M. J. 2021, arXiv e-prints, arXiv:2108.07818
Cordes, J. M., & Chatterjee, S. 2019, ARA&A, 57, 417
Day, C. K., Deller, A. T., Shannon, R. M., et al. 2020, arXiv e-prints, arXiv:2005.13162
Dehman, C., Viganò, D., Rea, N., et al. 2020, ApJL, 902, L32
Fung, P. K., & Kuijpers, J. 2004, A&A, 422, 817
Gajjar, V., Siemion, A. P. V., Price, D. C., et al. 2018, ApJ, 863, 2
Gil, J., Lyubarsky, Y., & Melikidze, G. I. 2004, ApJ, 600, 872
Goldreich, P., & Julian, W. H. 1969, ApJ, 157, 869
Herold, H. 1979, PhRvD, 19, 2868
Hessels, J. W. T., Spitler, L. G., Seymour, A. D., et al. 2019, ApJL, 876, L23
Ioka, K. 2020, ApJ, 904, 15
Kalapotharakos, C., Brambilla, G., Timokhin, A., Harding, A. K., & Kazanas, D. 2018, ApJ, 857, 44
Katz, J. I. 2014, PhRvD, 89, 103009
Kumar, P., & Bošnjak, Ž. 2020, MNRAS, 494, 2385
Kumar, P., Lu, W., & Bhattacharya, M. 2017, MNRAS, 468, 2726
Kumar, P., & Zhang, B. 2015, PhR, 561, 1
Kundu, E., & Zhang, B. 2021, MNRAS, 508, L48
Lin, L., Zhang, C. F., Wang, P., et al. 2020, Nature, 587, 63
Lorimer, D. R., Bailes, M., McLaughlin, M. A., Narkevic, D. J., & Crawford, F. 2007, Science, 318, 777
Lu, W., & Kumar, P. 2018, MNRAS, 477, 2470
Lu, W., Kumar, P., & Narayan, R. 2019, MNRAS, 483, 359
Lu, W., Kumar, P., & Zhang, B. 2020, MNRAS, 498, 1397
Luo, R., Wang, B. J., Men, Y. P., et al. 2020, Nature, 586, 693
Lyubarskii, Y. E. 1996, A&A, 308, 809
Lyubarskii, Y. E., & Petrova, S. A. 1998, A&A, 333, 181
Lyubarsky, Y. 2014, MNRAS, 442, L9
—, 2020, ApJ, 897, 1
—, 2021, Universe, 7, 56
Lyutikov, M. 2021a, arXiv e-prints, arXiv:2102.07010

- . 2021b, arXiv e-prints, arXiv:2110.08435
- Margalit, B., Beniamini, P., Sridhar, N., & Metzger, B. D. 2020, *ApJL*, 899, L27
- Melikidze, G. I., Gil, J. A., & Pataraya, A. D. 2000, *ApJ*, 544, 1081
- Melrose, D. B. 1978, *ApJ*, 225, 557
- . 2017, *Reviews of Modern Plasma Physics*, 1, 5
- Metzger, B. D., Margalit, B., & Sironi, L. 2019, *MNRAS*, 485, 4091
- Michilli, D., Seymour, A., Hessels, J. W. T., et al. 2018, *ArXiv e-prints*
- Muslimov, A. G., & Harding, A. K. 2004, *ApJ*, 606, 1143
- Pacholczyk, A. G. 1970, *Radio astrophysics. Nonthermal processes in galactic and extragalactic sources*
- Petroff, E., Hessels, J. W. T., & Lorimer, D. R. 2019, *A&A Rv*, 27, 4
- Philippov, A. A., & Spitkovsky, A. 2018, *ApJ*, 855, 94
- Plotnikov, I., & Sironi, L. 2019, *MNRAS*, 485, 3816
- Qiao, G. J., & Lin, W. P. 1998, *A&A*, 333, 172
- Qiao, G. J., Liu, J. F., Zhang, B., & Han, J. L. 2001, *A&A*, 377, 964
- Qu, Y., & Zhang, B. 2021, in preparation
- Rowe, E. T. 1995, *A&A*, 296, 275
- Ruderman, M. A., & Sutherland, P. G. 1975, *ApJ*, 196, 51
- Spitler, L. G., Scholz, P., Hessels, J. W. T., et al. 2016, *Nature*, 531, 202
- Thompson, C., & Duncan, R. C. 2001, *ApJ*, 561, 980
- Wadiasingh, Z., Beniamini, P., Timokhin, A., et al. 2020, *ApJ*, 891, 82
- Wang, J.-S., & Lai, D. 2020, *ApJ*, 892, 135
- Wang, W., Luo, R., Yue, H., et al. 2018, *ApJ*, 852, 140
- Wang, W., Zhang, B., Chen, X., & Xu, R. 2019, *ApJL*, 876, L15
- Wang, W.-Y., Yang, Y.-P., Niu, C.-H., et al. 2021, *ApJ*, submitted
- Xia, X. Y., Qiao, G. J., Wu, X. J., & Hou, Y. Q. 1985, *A&A*, 152, 93
- Xiao, D., Wang, F., & Dai, Z. 2021, *Science China Physics, Mechanics, and Astronomy*, 64, 249501
- Xu, R. X., Liu, J. F., Han, J. L. & Qiao, G. J. 2000, *ApJ*, 535, 354
- Yang, Y.-P., & Zhang, B. 2018, *ApJ*, 868, 31
- . 2020, *ApJ*, 892, L10
- . 2021, *ApJ*, 919, 89
- Yang, Y.-P., Zhu, J.-P., Zhang, B., & Wu, X.-F. 2020, *ApJL*, 901, L13
- Yuan, Y., Beloborodov, A. M., Chen, A. Y., & Levin, Y. 2020, *ApJL*, 900, L21
- Zhang, B. 2020, *Nature*, 587, 45
- Zhang, B., Hong, B. H., & Qiao, G. J. 1999, *ApJL*, 514, L111